

Computational Fluid Dynamics

Final Project Assignment

Design of Small-Scale Wind Tunnel

Version 1.0

Elias Olofsson (elol0076@student.umu.se)

Supervisor Krister Wiklund

Examiner Erik Zäll

Abstract

As evident, this report is not completed due to lack of time. Still I chose to hand it in regardless. For this, I apologize.

Contents

1	Introduction	1
2	Theory	1
3	Method	4
4	Results	7
5	Discussion	10
6	Conclusion	10
A	Appendix: Wind tunnel dimensions	15
B	Appendix: Contraction shape	17

1 Introduction

Introduction to the topic, with problem statement and aims of the investigation.

The report is organized as follows: Section 2 gives a short overview over the theoretical background and Section 3 describes the methods used in detail. In Section 4 the results are presented and then discussed in Section 5. Finally, Section 6 summarizes the results and presents the conclusions.

2 Theory

The dynamics of a viscous, incompressible fluid are governed by the Navier-Stokes equations [1] which relate the forces and momenta of the fluid continuum and enforce mass conservation, as per

$$\rho \frac{\partial u_i}{\partial t} + \rho(\mathbf{u} \cdot \nabla) u_i = -\frac{\partial p}{\partial x_i} + \frac{\partial \tau_{ij}}{\partial x_j} + f_i \quad (1)$$

$$\rho \nabla \cdot \mathbf{u} = 0, \quad (2)$$

where the density ρ is assumed to be constant, u_i is the velocity and f_i is any external force. Furthermore, the viscous stress tensor τ_{ij} is defined as

$$\tau_{ij} = 2\mu S_{ij} = \mu \left(\frac{\partial u_i}{\partial x_j} + \frac{\partial u_j}{\partial x_i} \right), \quad (3)$$

where μ is the dynamic viscosity of the fluid and S_{ij} is the rate of strain tensor. While in theory this partial differential equation (PDE) describes the full dynamics of any incompressible Newtonian fluid, in practice and especially within an engineering context [1] we tend to work with simplified, modelled versions of the full Navier-Stokes equations. One popular approach are the Reynolds Averaged Navier-Stokes (RANS) equations, which can be derived from Eq.1-3 using a Reynolds decomposition like

$$\begin{cases} u_i = U_i + u'_i \\ p = P + p' \\ \tau_{ij} = T_{ij} + \tau'_{ij} \end{cases}, \quad (4)$$

where lowercase variables are the instantaneous values, uppercase variables are the mean values and the primed quantities are the fluctuations from the mean. Substituting these decomposed variables into Eq.1 and taking the expectation value of the entire equation, we can simplify the PDE using statistical rules and eventually arrive at RANS, as per

$$\rho \left(\frac{\partial U_i}{\partial t} + U_j \frac{\partial U_i}{\partial x_j} \right) = -\frac{\partial P}{\partial x_i} + \frac{\partial T_{ij}}{\partial x_j} + \frac{\partial R_{ij}}{\partial x_j} + \langle f_i \rangle \quad (5)$$

$$\frac{\partial U_i}{\partial x_i} = 0 \quad \frac{\partial u'_i}{\partial x_i} = 0, \quad (6)$$

where we have defined the Reynolds stress R_{ij} as

$$R_{ij} \equiv \rho \langle u'_i u'_j \rangle, \quad (7)$$

and in analogue to Eq.3, the bulk viscosity stress is defined as

$$T_{ij} = \mu \left(\frac{\partial U_i}{\partial x_j} + \frac{\partial U_j}{\partial x_i} \right). \quad (8)$$

However, due to the 'left-over' primed velocities in the definitions of Reynolds stress Eq.7, the system of equations is not closed. Thus in order to solve RANS (Eq.5-6), we need closure of the problem by finding a way to model the Reynolds stress. One way of achieving this is by adopting the Boussinesq hypothesis [2], which models the Reynolds stress as

$$R_{ij} \equiv -\langle \rho u'_i u'_j \rangle = \mu_t \left(\frac{\partial U_i}{\partial x_j} + \frac{\partial U_j}{\partial x_i} \right) - \frac{2}{3} \rho k \delta_{ij}, \quad (9)$$

where δ_{ij} is the Kronecker delta, μ_t is defined as the turbulence viscosity and k is the turbulence kinetic energy, defined as

$$k \equiv \frac{1}{2} \langle u'_i u'_i \rangle. \quad (10)$$

Nonetheless, by adopting the Boussinesq hypothesis, we have not closed the system but rather moved the from the Reynolds stress tensor R_{ij} to the turbulent viscosity μ_t and the turbulence kinetic energy k . Thus, we need to choose a way to model these quantities, for which there are many options. The alternative we have chosen in here is the Low Re k- ε model [2], which employs the standard k- ε model with near wall modifications. The general form of the Low Re k- ε model is as per

$$\begin{aligned} \frac{Dk}{Dt} &= P_k - \tilde{\varepsilon} + D_k \\ \frac{D\tilde{\varepsilon}}{Dt} &= \frac{\tilde{\varepsilon}}{k} (f_1 C_{\varepsilon 1} P_k - f_2 C_{\varepsilon 2} \tilde{\varepsilon}) + D_\varepsilon + E, \end{aligned} \quad (11)$$

where P_k is defined as the production term of k ,

$$P_k \equiv \frac{R_{ij}}{\rho} \frac{\partial U_i}{\partial x_j} = \frac{\mu_t}{\rho} S^2. \quad (12)$$

Here, S^2 relates to the rate of strain S_{ij} as

$$S^2 \equiv 2S_{ij}S_{ij}, \quad (13)$$

and D_k is the diffusion of k

$$D_k \equiv \frac{\partial}{\partial x_j} \left[\frac{1}{\rho} \left(\mu + \frac{\mu_t}{\sigma_k} \right) \frac{\partial k}{\partial x_j} \right]. \quad (14)$$

The turbulence dissipation rate of k is defined as ε

$$\varepsilon \equiv \frac{\mu}{\rho} \left\langle \frac{\partial u'_i}{\partial x_j} \frac{\partial u'_i}{\partial x_j} \right\rangle, \quad (15)$$

which relates to $\tilde{\varepsilon}$ as per

$$\varepsilon = \tilde{\varepsilon} + D. \quad (16)$$

The term D_ε in Eq.11, which gives the diffusion of $\tilde{\varepsilon}$, is defined as

$$D_\varepsilon \equiv \frac{\partial}{\partial x_j} \left[\frac{1}{\rho} \left(\mu + \frac{\mu_t}{\sigma_\varepsilon} \right) \frac{\partial \varepsilon}{\partial x_j} \right], \quad (17)$$

and the turbulence viscosity model for the Low Re k- ε model is set to

$$\mu_t = f_\mu C_\mu \rho \frac{k^2}{\tilde{\varepsilon}}. \quad (18)$$

The constants $C_{\varepsilon 1}$, $C_{\varepsilon 2}$, $C_\mu \sigma_k$, σ_ε , E , D as well as the damping functions f_1 , f_2 , f_μ are typically inferred from experimental data, and there are many different alternative sets of constants and damping functions available. For this investigation, the chosen simulations software COMSOL implements the AKN model with the Low Re k- ε model, after its designers Abe, Kondoh, and Nagano [3] which specifies the damping functions as

$$\begin{aligned} f_\mu &= \left(1 - e^{-l^*/14}\right)^2 \left[1 + 5 \text{Re}_T^{-3/4} e^{-(\text{Re}_T/200)^2}\right] \\ f_1 &= 1 \\ f_2 &= \left(1 - e^{-l^*/3.1}\right)^2 \left[1 - 0.3e^{-(\text{Re}_T/6.5)^2}\right], \end{aligned} \quad (19)$$

where

$$l^* = \frac{\rho u_\varepsilon l_w}{\mu}, \quad \text{Re}_T \equiv \frac{\rho k^2}{\mu \varepsilon}, \quad u_\varepsilon = \left(\frac{\mu \varepsilon}{\rho}\right)^{1/4}, \quad (20)$$

in combination with the constants

$$C_{\varepsilon 1} = 1.5 \quad C_{\varepsilon 2} = 1.9 \quad C_\mu = 0.09 \quad \sigma_k = 1.4 \quad \sigma_\varepsilon = 1.4. \quad (21)$$

Simulations performed during this investigation have used initial conditions in the entire domain as

$$\mathbf{u} = 0, \quad p = 0, \quad (22)$$

while letting COMSOL set automatically the initial values for the turbulence kinetic energy k and the turbulence dissipation rate ε . I have unfortunately not been able to inspect manually which numerical value COMSOL chooses internally but my assumption is that it is either zero or a constant value close to zero.

For the inlet into the domain, I have specified the boundary condition to have a constant, normal velocity into the domain determined by the volumetric flow rate Q_{in} and the inlet surface area. The turbulence intensity of the incoming flow is set to 5% at the boundary, and COMSOL automatically sets the turbulence length scale, of which I similarly have not been able to gain insight into. The outlet boundary condition is a simple pressure constraint at zero pressure, while simultaneously suppressing any backflow. On all other surfaces of the domain, a no-slip condition $\mathbf{u} = 0$ is used.

Quantities used to quantify the flow within the simulations have been the turbulence intensity

$$I \equiv \frac{u'}{U} \quad (23)$$

where u' is the root mean square of the turbulent velocity fluctuations and U is the mean velocity of the flow. Furthermore, we use the dimensionless quantities

$$U^+ \equiv \frac{U}{u_\tau}, \quad (24)$$

and

$$y^+ \equiv \frac{\rho u_\tau y}{\mu}, \quad (25)$$

which is a scale free and universal quantity for flow near walls due to its usage of the friction velocity

$$u_\tau \equiv \sqrt{\tau_w/\rho}, \quad (26)$$

where τ_w is the wall shear stress. Similarly, we employ a dimensionless version of the turbulence kinetic energy k , as per

$$k^+ \equiv \frac{U}{u_\tau^2}. \quad (27)$$

Furthermore we have the Reynolds number

$$\text{Re} = \frac{\rho LU}{\mu}, \quad (28)$$

which balances the importance of the convective and viscous terms of the Navier-Stokes equations Eq.1, and its related quantity Re_τ based on the friction velocity, as per

$$\text{Re} = \frac{\rho L u_\tau}{\mu}, \quad (29)$$

3 Method

In this investigation, we have used fluid properties defined by Hydroflux AB, as given in Tab.1.

Table 1 – Fluid and flow properties used in the simulation, specified by Hydroflux AB.

Parameter	Value	Comment
Density	1.184 kg/m ³	Air 25°
Dynamic viscosity	$18.5 \cdot 10^{-6}$ Pas	Air 25°
Flow rate	0.05 m ³ /s	Determined by the choice of fan used to drive the flow
Turbulence intensity after settling chamber	1 – 5%	Depends on flow straightener, choice of screens, and the number of screens.

Any wind tunnel is composed of the same constituents components [4], a settling chamber with screens and/or honeycombs, a contraction section to increase velocity and uniformity of the flow, a testing chamber where the experiment takes place, a diffuser to recover static pressure and a drive system in the shape of a fan or turbine. The wind tunnel in question in this investigation is no exception, and the basic geometry of the wind tunnel was given by the Hydroflux AB as a CAD file, excluding the drive system of the wind tunnel, and is based on the design by S. Mauro *et. al.* [5], with help of J.E. Sargison *et. al.* [6] for the design of the contraction section. An overview of the wind tunnel can be seen in Fig.1.

Here, we have the settling chamber with a coarse comb used as a flow conditioner, which minimizes transverse flows and breaks up large-scale flow irregularities [4], followed by the contraction section. Flow is sped up in the contraction, which is designed to maximize flow

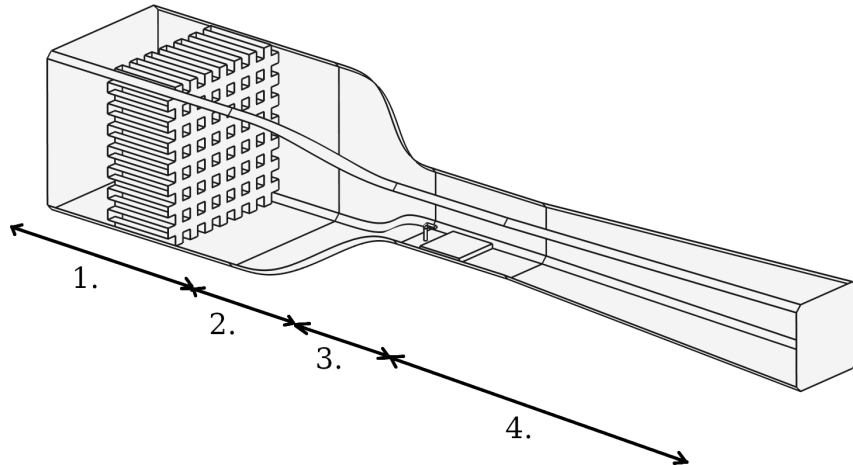


Figure 1 – Left to right in flow direction: 1. Settling chamber, 2. Contraction, 3. Test section with force sensor and smoke injector, 4. Diffuser. Original CAD design supplied by Hydroflux AB, improved with slight alteration of the contraction shape and with the addition of 45° chamfers along the four edges of the wind tunnel in the direction of flow.

uniformity at the test section entrance while minimizing boundary layer separation [6]. Following the contraction, the flow enters the test section where the aerodynamic experiment is taking place. In Fig.1 one can see the force sensor and the smoke injector placed in the test section. On the one hand the test section should be long enough in order for turbulence fluctuations to dampen down after the entrance, while on the other hand it should be short enough for boundary separation to not occur further down the test section [4]. Following the test section, the flow enters the diffuser which by its gradual widening reduces the flow-speed and decreases the pressure, which is beneficial and takes load of the drive system [4].

While the original geometry was supplied by Hydroflux AB, two slight changes to the wind tunnel design have been made in this investigation. Firstly, as discussed by S. Mauro *et. al.*[5], the optimal cross-sectional shape of the wind tunnel from a pure aerodynamic standpoint is for the tunnel to take a circular shape, which minimizes risks of flow separation at sharp edges. However, from a practical standpoint, a rectangular cross-sectional shape is much easier to construct and gives more surface area for experiments. A reasonable trade-off which [6] employs is to use 45° chamfers along the corners of the rectangular cross-section, and a similar approach has been used here in this investigation. Full details of the wind tunnel design and dimensions can be seen in Appendix A.

Secondly, a slight mistake was made in the original CAD-file supplied by Hydroflux AB. A small logical error in the Matlab-script for creation of the contraction shape in the wind tunnel resulted in the slight miss-alignment between the contraction section and the test section, yielding a small 'lip' at the intersection between test section and contraction. Since optimal conditions in the test section is minimal levels of turbulence and a uniform flow [4], such a small non-streamlined irregularity will have the possibility of creating unwanted flow separation and a boundary layer build-up in the test section. To validate these claims, tests were made to compare the performance of the empty wind tunnel using both the original and the modified design. All further investigations in this study have been performed using the modified design.

Derived quantities from the performed simulations in this investigation have been taken from an assortment of cut-planes, cut-lines and cut-points at different locations within the wind tunnel.

Velocity and turbulence intensity surface plots have been taken along 3D cut-planes as shown in Fig.2. The reason for using two cut-planes parallel to the flow was to be able to see the velocity

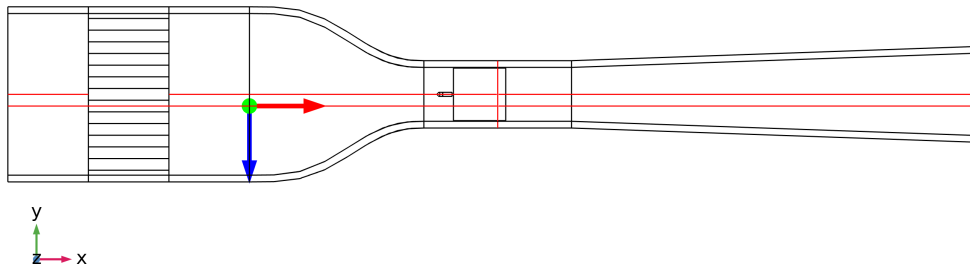


Figure 2 – Cut-planes used for gathering of flow quantities. The two parallel cut-planes enabled graphing of quantities both in the small ducts of the flow comb in the settling chamber and at the center-line of the smoke injector.

and turbulence intensity within the small ducts of the rectangular comb of the settling duct, but to also graph the cross-section of the smoke injector centered in the wind tunnel. This proved to be a valid approach since differences were small in plotted quantities of the two parallel cut-planes. A third plane was placed perpendicular to the flow at the center of the test section.

For graphing the difference between the empty wind tunnel flow and with the force sensor and smoke injector added, three vertical cut-lines were used in the test section, as seen in Fig.3. They were placed along the center-line of the wind tunnel following the flow, and spaced out at 0.25, 0.5 and 0.75 times the length of the test section. The cut-points used for data-gathering

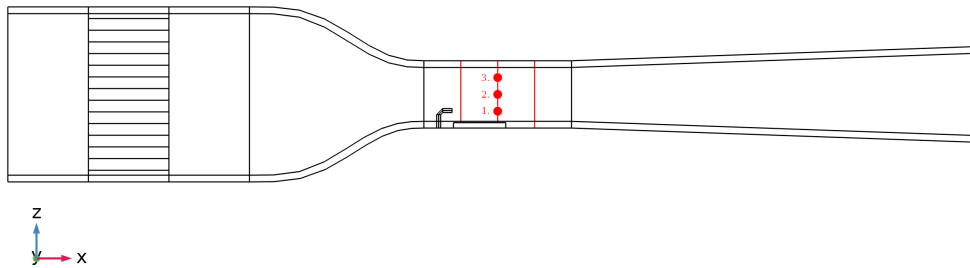


Figure 3 – Cut-lines and cut-points used for gathering of flow quantities. Both the vertical cut-lines and the cut-points are centered in the transverse direction of the wind tunnel.

during the mesh convergence test can be seen in Fig.3, which are centered in the transverse orientation of the flow, ordered vertically at the center of the test section, vertically spaced at 0.25, 0.5 and 0.75 times the height of the test section.

During the comparison of simulations of the flow with the sensor, with the smoke injector and with an empty tunnel, the mesh used employed a global maximum element size of 0.0171 m, with a locally enforced maximum element size of 0.00698 m at all boundaries within the test section. In addition, all boundaries were specified to use 6 boundary layers with a thickness adjustment factor of 2, and locally constrained to use 10 boundary layers and a thickness adjustment factor of 1 at all boundaries within the test section. This gave me a simulation time around 40 min using a stationary 4 core computer.

For the mesh convergence test, which was performed with an empty wind tunnel using the modified geometry, the maximum element size was set to 0.0132m times a parameter `meshtest`, and for the local constraint at all boundaries within the test section, a maximum element size of

0.005235 m times a parameter `meshtest`. Then two consecutive batch sweeps were performed over the parameter `meshtest`, first in the range 1.0 to 3.0 in 10 linearly spaced increments, and later from 1.0 to 1.4 in 17 linearly spaced steps.

During this study, I did not experience poor convergence while running the simulations, which I believe could be due to usage of the 'automatic' wall treatment feature in COMSOL, which smoothly switches between the Low Re $k-\varepsilon$ model and the standard $k-\varepsilon$ model with wall functions, depending on the local mesh resolution. Normally, the Low Re $k-\varepsilon$ model requires a relatively fine mesh in order to have good convergence properties and one would have to increase the mesh quality when experiencing poor convergence. However, this never was a concern during this study.

4 Results

Firstly, due to reasons presented in Sec.3, the modifications to the original wind tunnel design provided by Hydroflux AB must be justified and validated. Two simulation runs performed at a high mesh quality as specified in Sec.3 were performed for each of the two geometries; the original and the modified design. The velocity profile of the original Hydroflux design can be seen in Fig.4, graphed along the slightly off-center cut-plane parallel to the flow as well as through the cut-plane perpendicular to the flow at the center of the test section. As one can see

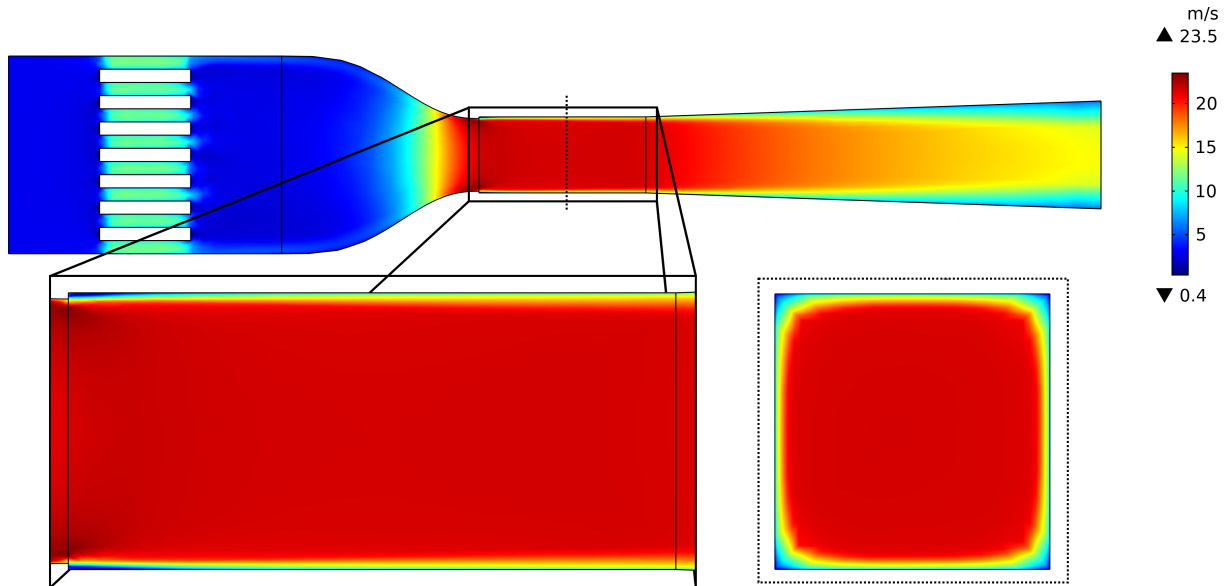


Figure 4 – Cut-planes showing velocity magnitude for the original geometry.

in the figure, the flow forms a small separation bubble [1] as it passes over the small 'lip' at the intersection between the contraction and the test section. This generates a small boundary layer which propagates down the test section, widening as it travels downstream. Furthermore, in the cut-plane perpendicular to the flow, one can note that the square edges of the rectangular cross-section of the wind tunnel seem to be a source of flow slow-down and separation, as predicted by [6].

Next, we graph the turbulence intensity for the original geometry, as seen in Fig.5. Here, one

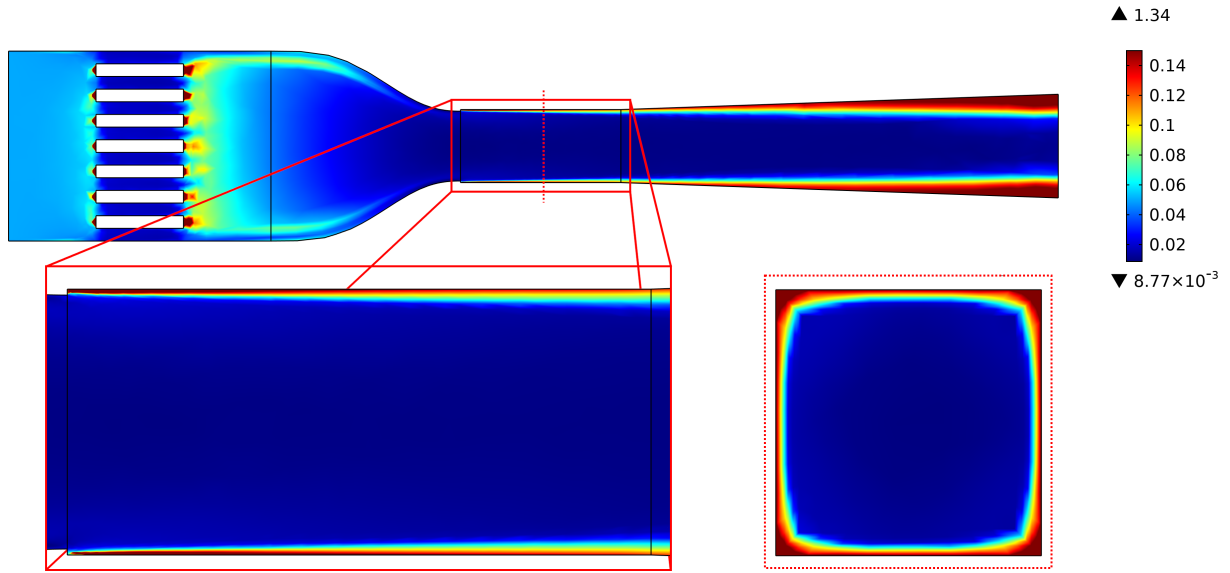


Figure 5 – Cut-planes showing turbulence intensity for the original geometry.

can see the creation of turbulence generated by the small 'lip' between the contraction and the test section, as well as at the square corners of the wind tunnel cross-section perpendicular to the flow.

For the second simulation, we run on an equivalent mesh the modified design, as specified in Sec.3 and in Appendix A-B. Cut-planes of the velocity magnitude can be seen in Fig.6, also plotted along the slightly off-center cut-plane parallel to the flow and perpendicular to the flow. Here, one can see a decrease in boundary layer separation, likely due to the removal of the slight

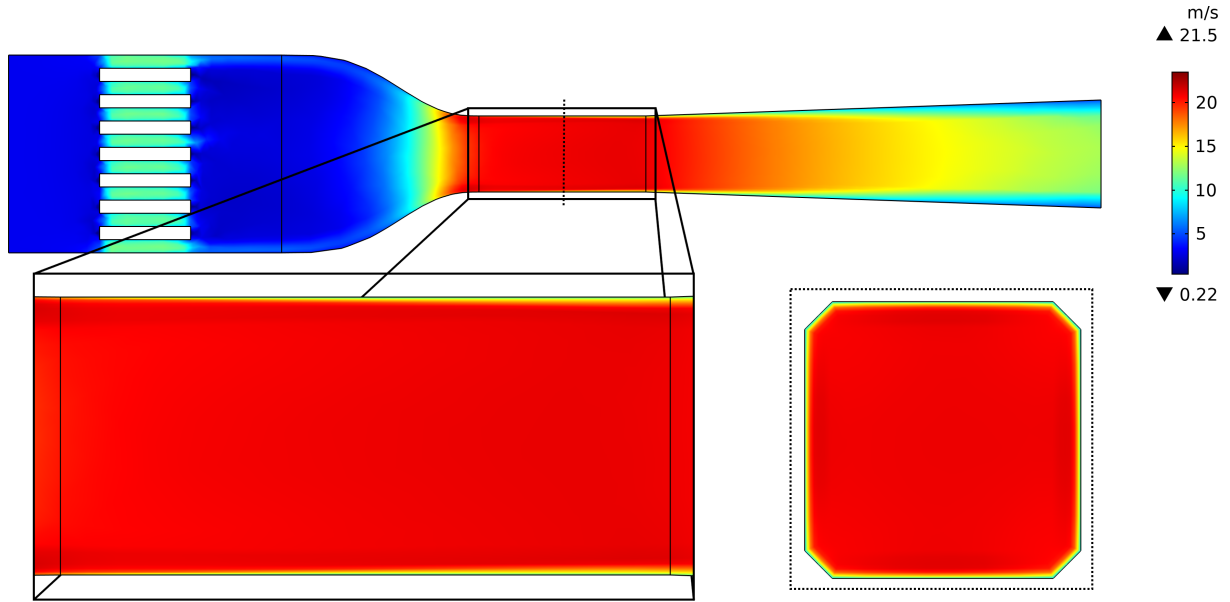


Figure 6 – Cut-planes showing velocity magnitude for the modified geometry.

'lip' at the intersection between contraction and test section of the original design. Additionally, the flow separation at the square corners of the perpendicular cross-section of the wind tunnel have been dramatically reduced, likely due to the introduction of 45° chamfers along the wind tunnel corners.

Moreover, we can see in the equivalent graph of the turbulence intensity along the cut-planes, as seen in Fig.7, that turbulence levels have decreased relative to the original design. The boundary

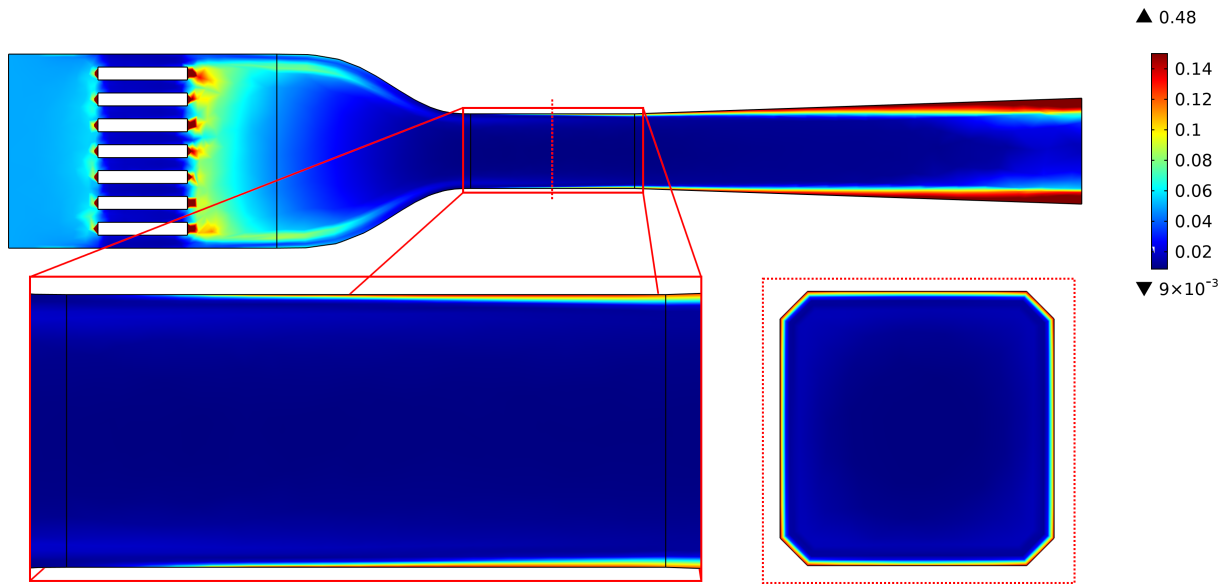


Figure 7 – Cut-planes showing turbulence intensity for the modified geometry.

layer with turbulence is thinner than in the original geometry, and additionally that turbulence levels have lowered in the corners of the wind tunnel cross-section.

As such, all further investigations conducted in this study have been performed with the modified geometry, which included the introduction of 45° chamfers and a slight error-correction in the shape of the contraction section which eliminated a small miss-alignment between the the contraction and test section.

In order to determine if a given solution to a simulation is representative of the theoretical 'exact' solution, a mesh convergence study is performed. Here the given simulation is re-run a number of times with different quality and coarseness of its mesh, and we study the convergence of some given parameters within the simulation. For this study, the reference case of an empty tunnel was chosen, and the quantities inspected in each solution was the velocity magnitude U and pressure P at the three cut-points as specified in Sec.3. The result of the mesh convergence study can be seen in Fig.8. Here, one can see how the plotted quantities seem to stagnate as the number of degrees of freedom increases, as to be expected. For the final comparison between the empty tunnel, with the force sensor added and with the smoke injector added, the finest mesh in this study, or finer, was used.

To address the aim of this investigation and see how the wind tunnel flow changes as one adds the force sensor and smoke injector, three further simulations were conducted at the finest mesh. First, a reference case with an empty wind tunnel, second a case with the smoke injector and thirdly a case with only the smoke injector.

The results of

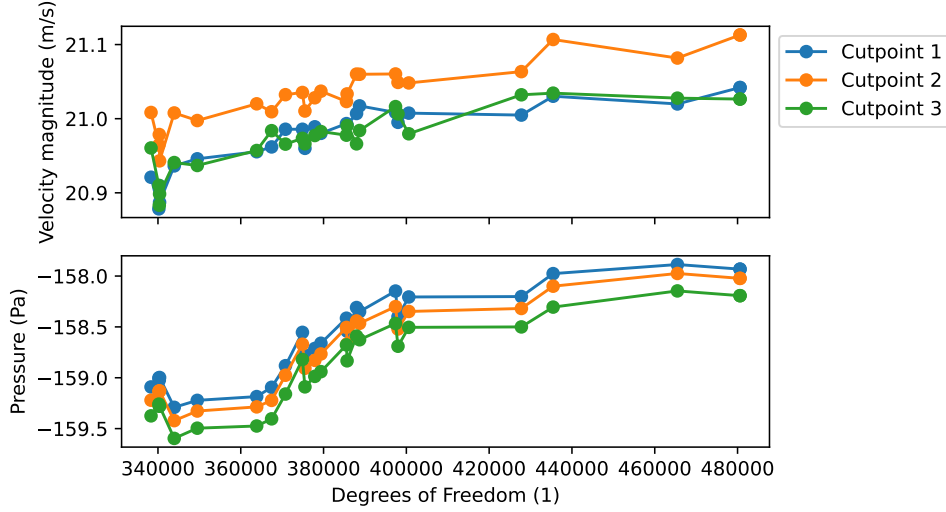


Figure 8 – Mesh convergence study over two sequential batch sweeps. Quantities graphed in cut-points as specified in Sec.3.

5 Discussion

Text goes here.

6 Conclusion

Text goes here.

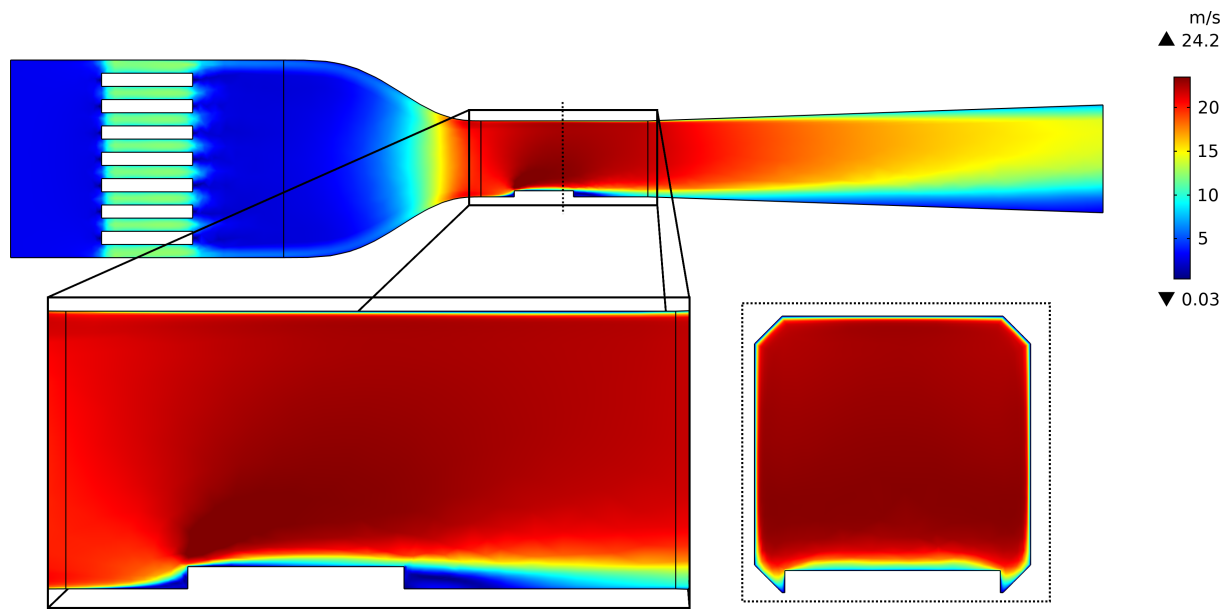


Figure 9 – Velocity magnitude, sensor added.

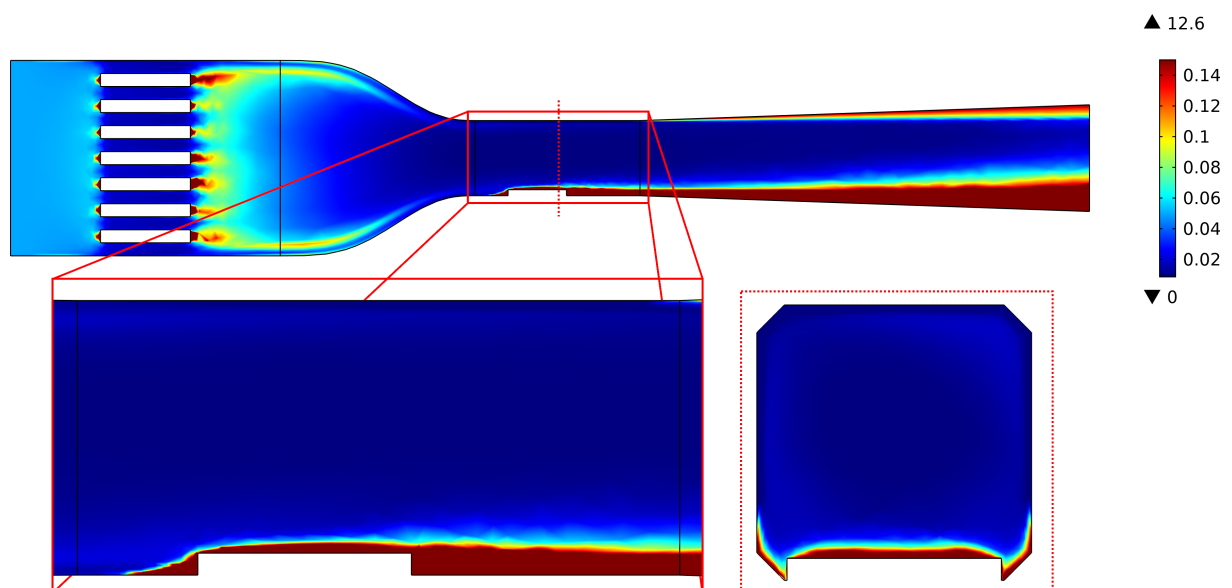


Figure 10 – Turbulence intensity, sensor added.

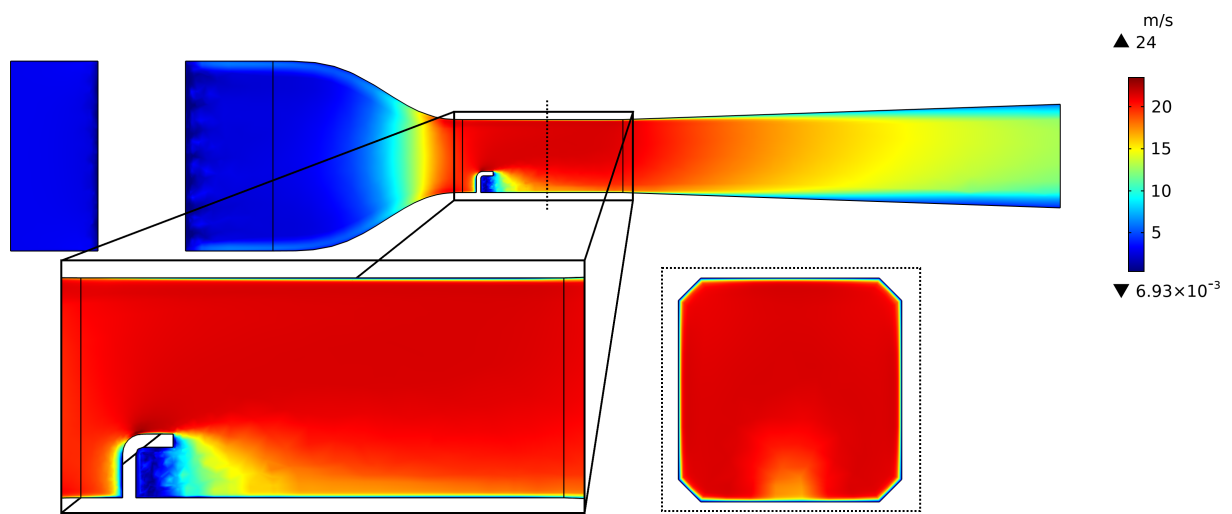


Figure 11 – Velocity magnitude, injector added.

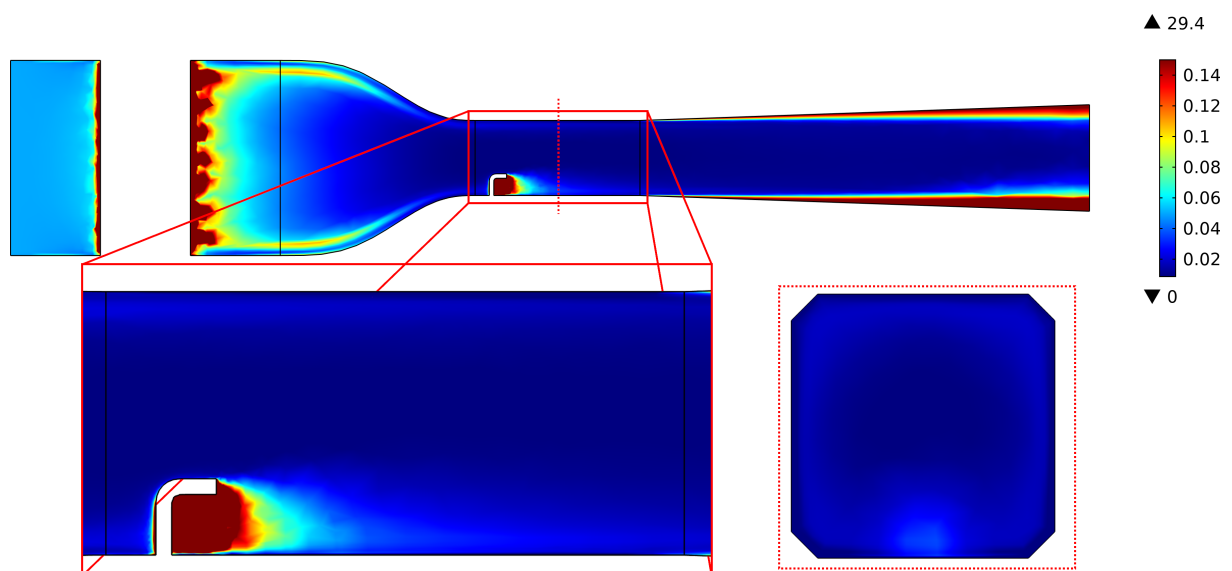


Figure 12 – Turbulence intensity, injector added.

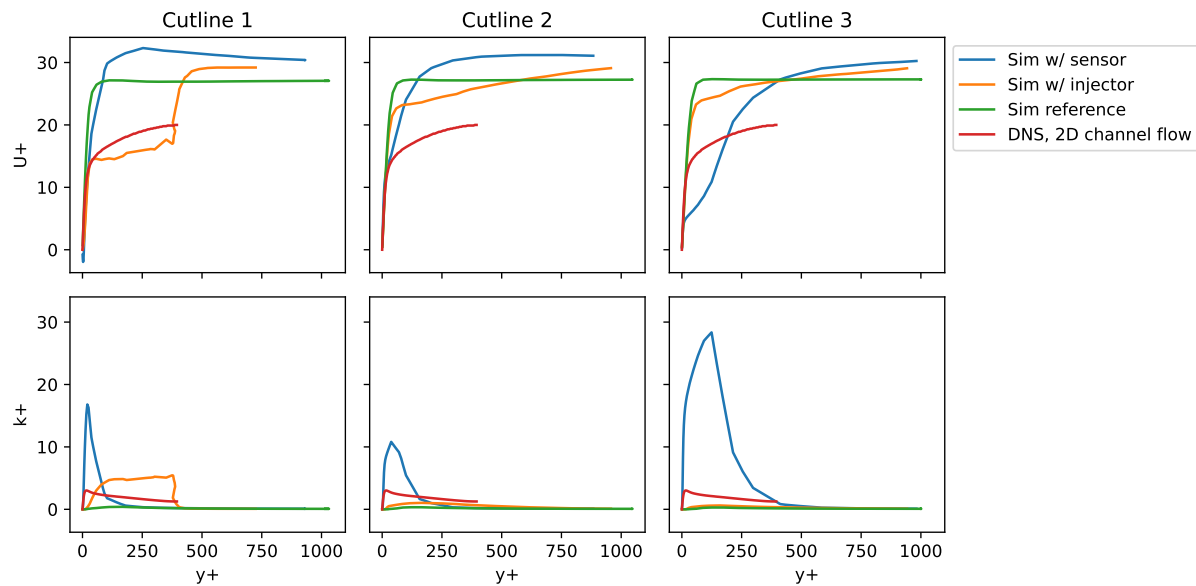


Figure 13 – Comparison along cutlines.

References

- [1] P. A. Davidson, *Turbulence: an introduction for scientists and engineers*, Second edition. Oxford, United Kingdom ; New York, NY, United States of America: Oxford University Press, 2015, 630 pp., OCLC: ocn911091654.
- [2] F. G. Schmitt, “About boussinesq’s turbulent viscosity hypothesis: Historical remarks and a direct evaluation of its validity,” *Comptes Rendus Mécanique*, vol. 335, no. 9, p. 617, Oct. 2007. DOI: 10.1016/j.crme.2007.08.004.
- [3] K. Abe, T. Kondoh, and Y. Nagano, “A new turbulence model for predicting fluid flow and heat transfer in separating and reattaching flows—i. flow field calculations,” *International Journal of Heat and Mass Transfer*, vol. 37, no. 1, pp. 139–151, Jan. 1, 1994. DOI: 10.1016/0017-9310(94)90168-6.
- [4] L. Cattafesta, C. Bahr, and J. Mathew, “Fundamentals of wind-tunnel design,” in *Encyclopedia of Aerospace Engineering*, R. Blockley and W. Shyy, Eds., Chichester, UK: John Wiley & Sons, Ltd, Dec. 15, 2010, eae532. DOI: 10.1002/9780470686652.eae532.
- [5] S. Mauro, S. Brusca, R. Lanzafame, F. Famoso, A. Galvagno, and M. Messina, “Small-scale open-circuit wind tunnel: Design criteria, construction and calibration,” *International Journal of Applied Engineering Research*, vol. 12, no. 23, pp. 13 649–13 662, 2017.
- [6] J. Sargison, G. Walker, and R. Rossi, “Design and calibration of a wind tunnel with a two dimensional contraction,” presented at the 15th Australasian Fluid Mechanics Conference, The University of Sydney, Sydney, Australia: University of Tasmania, Dec. 13, 2004.

A Appendix: Wind tunnel dimensions

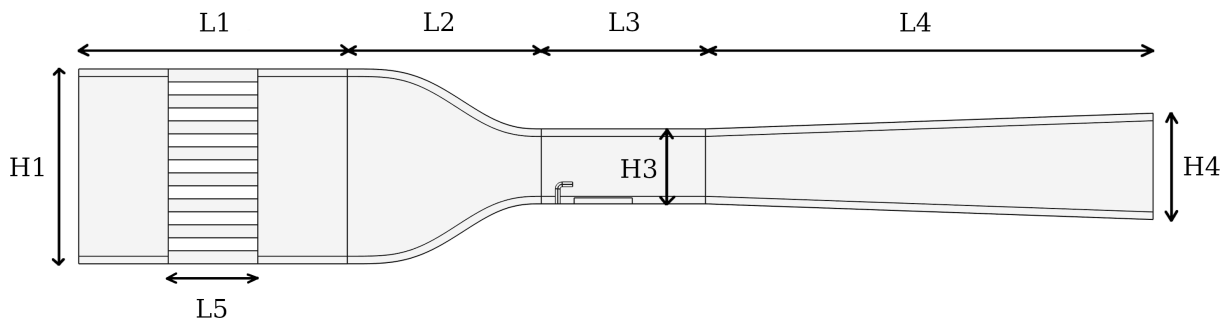


Figure A.1 –Caption.

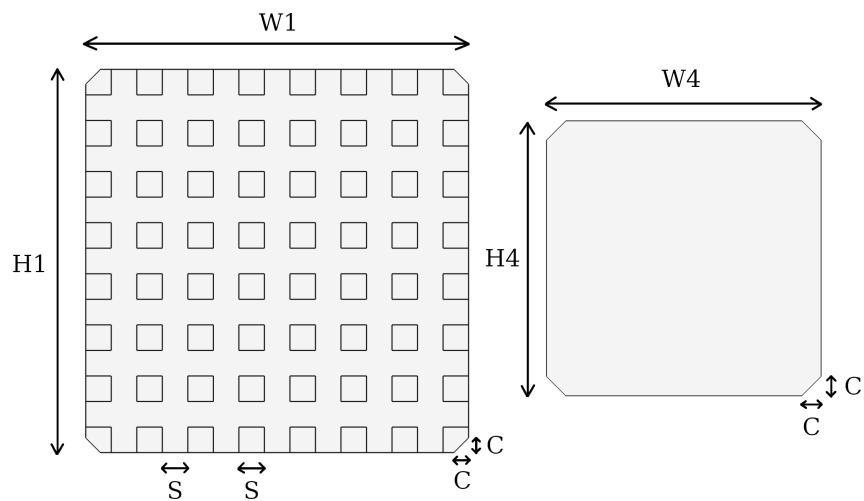


Figure A.2 –Caption.

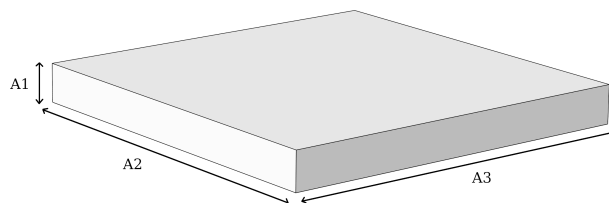
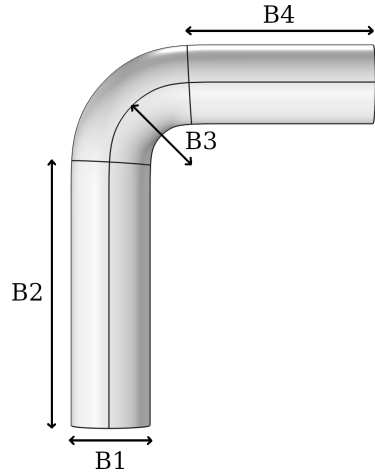


Figure A.3 –Caption.

**Figure A.4** – Caption.**Table A.1** – Caption. NEED TO VERIFY ALL VALUES HERE.

Dimension	Size [mm]	Comment
L1	180	Length of settling chamber
L2	130	Length of contraction
L3	110	Length of test section
L4	300	Length of diffuser
L4	60	Length of flow settling comb
H1	130	Height of inlet to the settling chamber
H3	50	Height of inlet to test section
H4	71	Height of outlet from diffuser
W1	130	Width of settling chamber
W3	50	Width of test section
W4	71	Width of diffuser at outlet
S	1/15*H1	Element width of flow settling comb
C	5	Width of 45° chamfer

Table A.2 – Caption.

Dimension	Size [mm]	Comment
A1	4	Force sensor height
A2	39	Force sensor depth
A3	39	Force sensor length
B1	3	Injector diameter
B2	10	Injector vertical length
B3	3	Injector bend radius
B4	10	Injector horizontal length

B Appendix: Contraction shape

$$y = ax^6 + bx^5 + cx^4 + dx^3 + ex^2 + fx + g \quad (30)$$

Table B.1 – Caption.

Parameter	Original design	Improved design	Comment
CR	7	6.76	Contraction ratio
a	$-7.6770 \cdot 10^4$	$-8.2870 \cdot 10^4$	
b	$2.4374 \cdot 10^4$	$2.5856 \cdot 10^4$	
c	$-2.0152 \cdot 10^3$	$-2.1008 \cdot 10^3$	
d	$3.3626 \cdot 10^{-12}$	$-2.0664 \cdot 10^{-13}$	
e	0	0	
f	0	0	
g	-	-	Vertical offset

```

clear all
% Script based on the original work provided by Hydroflux AB.
% Modified by Elias Olofsson.
%
% Changelog:
% v1.0 2021-12-05: Author: Hydroflux AB.
%   Publication of original work.
% v2.0 2022-01-14: Author: Elias Olofsson.
%   Changed order of operations such to make flush connections with settling
%   chamber and test section of predetermined widths. Now CR is determined by
%   the ratio of Di to Do, where in the previous version, Di where allowed
%   to vary to fit a certain specified value of CR.
%
% Design of wind tunnel contraction shape based on the following two papers:
% [1] "Design and calibration of a wind tunnel with a two dimensional
% contraction", J.E. Sargison, G.J. Walker and R. Rossi, 2004
% [2] "Flow characteristics in low-speed wind tunnel contractions: Simulation and
% testing", Alexandria Engineering Journal (2018) 57
% Following [1] a sixth order polynom is chosen as shape model for a
% 2D-contraction with inlet crosssection Di*W, outlet crosssection Do*W:
%  $y=a*x^6+b*x^5+c*x^4+d*x^3+e*x^2+f*x+g$ 
% From [2] the recommendation of contraction number CR is between 6-12
% and the contraction length L is between  $0.75*Di$  and  $1.25*Di$ 
% CR is chosen to 5, i.e.  $CR=(Di*W)/(Do*W)=5$ 
% and the contraction length is chosen to  $L=Di$ 
% Model 3 in [1] is chosen, i.e  $xi/L=0.6$  and  $\alpha=0$ , where xi is the
% inflection point along contraction axis and alpha is the inlet curvature.

Do=0.050; %50mm
Di=0.130; %130mm
CR = Di^2/Do^2
L=1.0*Di;
xi=0.6*L;
h=1*(Di/2-Do/2);

% The constraints on the shape model is the following:
% x=0: y(0)=h, y'(0)=0, y''(0)=0
% x=L: y(L)=0, y'(L)=0, y''(L)=0
% x=xi: y''(xi)=0
% When the constraints are applied we obtain a system of equations
% for the coefficients a,b,c,d in terms of L and xi, and that g=h, f=e=0.
% The system looks like Asys*Coeff=B:

Asys=[30*xi^4 20*xi^3 12*xi^2 6*xi;
L^6 L^5 L^4 L^3;
6*L^5 5*L^4 4*L^3 3*L^2;
30*L^4 20*L^3 12*L^2 6*L];

```

```
B=[0 -h 0 0]';
Coeff=linsolve(Asys,B);
a=Coeff(1); b=Coeff(2); c=Coeff(3); d=Coeff(4); e=0; f=0; g=h;
%Contraction shape model from [1]
x=[0:0.001:L];
y=a*x.^6+b*x.^5+c*x.^4+d*x.^3+e*x.^2+f*x+g;

%Plot shape
figure(1)
hold on
plot(x,y+Do/2,'b')
plot(x,-y-Do/2,'b')
xlabel('x'); ylabel('y'); axis equal
title(['CR=', num2str(CR), ', L/Di=', num2str(L/Di)])
```